



ORIGINAL ARTICLE

Label-free electrochemical biosensor with magnetically induced self-assembly for the detection of cancer antigen 125



Yao Yue^{a,1}, Xiu Chen^{b,1}, Jie Wang^a, Mingyi Ma^a, Aolin He^{c,*}, Ruijiang Liu^{a,*}

^a School of Pharmacy, Jiangsu University, Zhenjiang 212013, PR China

^b The People's Hospital of Danyang, Affiliated Danyang Hospital of Nantong University, Zhenjiang 212300, PR China

^c Affiliated Kunshan Hospital, Jiangsu University, Suzhou 215300, PR China

Received 27 January 2023; accepted 10 June 2023

Available online 16 June 2023

KEYWORDS

Ovarian cancer;
Cancer antigen 125;
Mg_{0.5}Cu_{0.5}Fe₂O₄-Au
nanocomposites;
Magnetic self-assembly;
Label-free electrochemical
biosensor

Abstract Magnetically induced self-assembly technology was used to construct a label-free electrochemical biosensor based on magnetic Mg_{0.5}Cu_{0.5}Fe₂O₄-Au nanocomposites for the sensitive detection of cancer antigen 125 (CA125). To aim for this, Mg_{0.5}Cu_{0.5}Fe₂O₄ nanoparticles were first prepared via the rapid combustion process. The average diameter of the nanoparticles calcined at 800 °C with the absolute ethanol volume of 20 mL was about 169.3 nm. Then Au was used for the surface modification by NaBH₄ reduction reaction approach. The magnetic glassy carbon electrode (MGCE) was modified by Mg_{0.5}Cu_{0.5}Fe₂O₄-Au via a magnetic induction self-assembly process. The reduced thiol-modified single-stranded DNA was attached to the Mg_{0.5}Cu_{0.5}Fe₂O₄-Au nanocomposites by Au-S bonds without any coupling agent. CA125 antigen was grabbed directly by its aptamer DNA due to its specific identification with the aptamer. Finally, the modified electrodes were blocked with BSA and then characterized. Finally, DPV analysis was used for CA125 detection, the novel fabricated biosensor demonstrated good detection properties for CA125 with a linear range of 5–125 U/mL and a detection limit of 4.4 U/mL. The results showed that the aptamer sensor had good specificity, repeatability, and stability. The feasibility of our sensor for the determination of CA125 was also demonstrated by measuring CA125 levels in serum using the Roche gold-standard instrument of the People's Hospital of Danyang as the reference value. The recoveries of real serum samples were 94.65–101.71%, and RSDs were 1.26–4.65%. Moreover, the surface of the electrode could be cleaned and reused by magnetic separation, greatly

* Corresponding authors at: School of Pharmacy, Jiangsu University, Zhenjiang 212013, PR China (R. Liu). Affiliated Kunshan Hospital, Jiangsu University, Suzhou 215300, PR China (A. He).

E-mail addresses: aolinhe@163.com (A. He), luckystar_lrj@ujs.edu.cn (R. Liu).

¹ These authors have contributed equally to this work and share the first authorship.

Peer review under responsibility of King Saud University.



Production and hosting by Elsevier

reducing the cost and providing the possibility for a point-of-care test (POCT). This work demonstrated a new strategy for integrating both nanostructures and biocompatibility to build advanced cancer biomarker sensors with wide applications.

© 2023 The Author(s). Published by Elsevier B.V. on behalf of King Saud University. This is an open access article under the CC BY-NC-ND license (<http://creativecommons.org/licenses/by-nc-nd/4.0/>).

1. Introduction

Ovarian cancer as the most fatal gynecologic cancer type has attracted worldwide attention in recent years (Franier and Thompson, 2019; Nash and Menon, 2020). According to statistics, an estimated 313,959 new ovarian cancer cases and 207,252 deaths because of ovarian cancer were reported in the world in 2020 (Sung et al., 2021). Cancer antigen 125 (CA125) (Giamougiannis et al., 2021; White et al., 2022; Lai et al., 2022), commonly found in the serum of patients with epithelial ovarian tumors (serous tumors), is normally below 35 U/mL (Al-Ogaidi et al., 2014). Serum CA125 is of great significance in monitoring the condition of epithelial ovarian cancer. Epithelial ovarian cancer can be completely resolved in a short period after treatment. In numerous pieces of research, it was found that early-stage cancer has a 5-year overall survival of 92% (Zhang et al., 2021a). The serum CA125 test can detect relapse early and treat it early. CA125 is the most widely used serum marker for preoperative diagnosis of ovarian cancer (Zhang et al., 2022a). Conventional affinity assays are limited by low specificity due to the heterogeneity in the structure and molecular nature of CA125 (Sadasivam et al., 2020). Therefore, improving the specificity of CA125 in the diagnosis of early epithelial ovarian cancer has become the key.

To overcome the low specificity of CA125, new affinity-based assays need to be developed to improve specificity without reducing sensitivity. Aptamer biosensors utilize the specific recognition between DNA-aptamer and target substances to detect the substances (Zhang et al., 2021b). They can effectively identify DNA (Liu et al., 2021), proteins (Zhao et al., 2022), cells (Peng et al., 2022), metal ions (Yu et al., 2022; Ebrahimi et al., 2022; Jin et al., 2023), biological molecules (Bi et al., 2023), and other substances (Li et al., 2023). The use of aptamers as biological recognition elements has the advantages of high specificity and good sensitivity. In this study, an electrochemical biosensor based on DNA-aptamer is designed to detect ovarian cancer tumor marker CA125.

Magnetic nanomaterials (NMs) have the advantages of easy recycling, low pollution, economy, environmental protection, high electrocatalytic activity, large specific surface area, and easy functionalization. At present, NMs and their composites have been widely applied in the construction of electrochemical biosensors (Reverté et al., 2016; Negahdary and Angnes, 2022). To improve the conductivity of electrochemical sensors, various materials have been developed and used to modify the NMs. Among them, Gold (Au) is widely used to modify the NMs to form Au-coated nanocomposites owing to its good stability, electrochemical, optical, electromagnetic, and catalytic properties (Sun et al., 2022; Liu et al., 2023). Moreover, Au and sulfhydryl modified DNA-aptamer can be assembled via the Au-S bond, thus creating a biocompatible environment (Pumera et al., 2007; Malekzad et al., 2017).

The $\text{Mg}_{0.5}\text{Cu}_{0.5}\text{Fe}_2\text{O}_4$ nanoparticles (NPs) are promising nanomaterials, and there is no research on the use of $\text{Mg}_{0.5}\text{Cu}_{0.5}\text{Fe}_2\text{O}_4$ for CA125 determination. Magnetic $\text{Mg}_{0.5}\text{Cu}_{0.5}\text{Fe}_2\text{O}_4$ NPs have superparamagnetism, which can be magnetically separated by an external magnetic field to achieve pre-enrichment of the object to be measured, and also be magnetically self-assembled onto a magnetic glassy carbon electrode (MGCE) without adding any crosslinking agent, which is simple and fast to operate (Ahmadi et al., 2021; Low et al., 2021). Compared with $\alpha\text{-Fe}_2\text{O}_3/\text{Fe}_3\text{O}_4$ nanomaterials (Ni et al., 2022) prepared by Ni et al., there is no problem of oxidative demagnetization.

MGCE has the advantages of high electrical conductivity, good stability to chemicals, no gas passing through the electrode, high purity, wide potential window, and cheap and easy to obtain. The main advantages of MGCE are reflected in regeneration and easy use, which has become a hot research topic in the field of electrochemical biosensors (Asghar et al., 2020; Liu et al., 2019). The surface of the electrode can be cleaned by magnetic separation and reused, thus greatly reducing the cost and providing the possibility for a clinical point of care test (POCT).

In this work, magnetic $\text{Mg}_{0.5}\text{Cu}_{0.5}\text{Fe}_2\text{O}_4\text{-Au}$ nanocomposites (NCs) were used as signal amplifiers, combined with magnetic induction self-assembly technology, based on the specific identification of CA125 and aptamer DNA, a label-free electrochemical aptamer sensor was developed and its detection performance was evaluated.

2. Experimental

2.1. Preparation of magnetic $\text{Mg}_{0.5}\text{Cu}_{0.5}\text{Fe}_2\text{O}_4\text{-Au}$ nanocomposites

Firstly, $\text{Mg}_{0.5}\text{Cu}_{0.5}\text{Fe}_2\text{O}_4$ NPs were prepared via a rapid combustion process. Typically, 1.18 g magnesium nitrate hexahydrate, 1.11 g cupric nitrate trihydrate, and 7.47 g ferric nitrate nonahydrate were dispersed in different volumes (20, 30, 40, 50, and 100 mL) of absolute ethanol, magnetically stirred for 30 min, the ternary homogeneous solutions were poured into the crucible and ignited to burn. After combustion, the precursors were calcined at various temperatures (400, 500, 600, 700, and 800 °C) with a heating rate of 3 °C/min to obtain $\text{Mg}_{0.5}\text{Cu}_{0.5}\text{Fe}_2\text{O}_4$ NPs. And the NPs were characterized by Rigaku D/max 2500 PC XRD with $\text{Cu-K}\alpha$ radiation, the morphology and composition analyses were investigated with SEM and TEM, and the magnetic measurements were taken on an ADE DMS-HF-4 VSM.

$\text{Mg}_{0.5}\text{Cu}_{0.5}\text{Fe}_2\text{O}_4\text{-Au}$ NCs were prepared by the NaBH_4 reduction method. 1 g of polyethyleneimine (PEI) was added to double distilled water of 100 mL and magnetically stirred for 30 min. Then 50 mg $\text{Mg}_{0.5}\text{Cu}_{0.5}\text{Fe}_2\text{O}_4$ NPs were put into the PEI solution, dispersed 30 min by ultrasound, and heated in a 90 °C water bath for 1 h, and $\text{Mg}_{0.5}\text{Cu}_{0.5}\text{Fe}_2\text{O}_4\text{-PEI}$ intermediates were obtained by post-processing (centrifuging at 10000 rpm, washing 3 times with double distilled water, drying at 50 °C and grinding). Followed by, 10 mg $\text{Mg}_{0.5}\text{Cu}_{0.5}\text{Fe}_2\text{O}_4\text{-PEI}$ intermediates were ultrasonically dispersed in 150 mL double distilled water, and 1 mL of 20 mg/mL chloroauric acid hydrated (HAuCl_4) was added and ultrasonically dispersed in an ice bath for 30 min. Finally, 9 mL of 0.075% NaBH_4 solution was slowly added within 2 min, and mechanically stirred in an ice bath. $\text{Mg}_{0.5}\text{Cu}_{0.5}\text{Fe}_2\text{O}_4\text{-Au}$ NCs were gained after the same post-processing and characterized by EDS, which was used in conjunction with TEM to analyze the elements, mass percentages (wt%), and atomic percentage contents (at %), scanned the element distribution of the whole surface and estimated the enrichment area of elements.

2.2. Construction of label-free electrochemical biosensor

The electrochemical aptamer sensor electrode modification process was verified using cyclic voltammetry (CV) and electrochemical impedance spectroscopy (EIS) analyses on a CHI660E (China) electrochemical workstation. The CV parameters were -0.2 V to 0.7 V, and the scanning rate was 100 mV/s. The EIS parameters were 0.01 Hz– 10 kHz and the signal amplitude was 5 mV.

Before modification, the MGCE was polished with 0.3 μm and 0.05 μm alumina, then ultrasonically cleaned the electrode twice and rinsed with ultrapure water. Sulfhydryl groups modified DNA aptamer (5'-SH-AAAAACTACTATAGGGA GACAAGAATAAACGCTCAA-3') was supplied by Sangon Biotechnology Co., Ltd. (Shanghai, China) and Genscript Biotechnology Co., Ltd. (Nanjing, China) (Sadasivam et al., 2020).

To modify the MGCE, different concentrations of $\text{Mg}_{0.5}\text{Cu}_{0.5}\text{Fe}_2\text{O}_4$ -Au NCs (5 – 25 mg/mL) were dropped onto the electrode surface to make the NCs attraction onto the electrode by magnetic self-assembly and then dried at room temperature for 2 h. To attach DNA to the surface of $\text{Mg}_{0.5}\text{Cu}_{0.5}\text{Fe}_2\text{O}_4$ -Au NCs, DNA of various concentrations (4 – 12 μM) was dropped on the electrode surface and incubated overnight at 4 $^\circ\text{C}$. Buffer TCEP effectively reduced the disulfide bond formed by the sulfhydryl groups at the 5' end of DNA, keeping the DNA in a single strand structure. DNA was connected to the surface of $\text{Mg}_{0.5}\text{Cu}_{0.5}\text{Fe}_2\text{O}_4$ -Au NCs through Au-S bond and obtained MGCE/ $\text{Mg}_{0.5}\text{Cu}_{0.5}\text{Fe}_2\text{O}_4$ -Au/DNA after air-dried. The modified electrode was finally blocked with 8 μL of BSA (0.25%) and incubated at 4 $^\circ\text{C}$ for 30 min.

For the label-free determination of CA125, the CA125 antigen was incubated at 37 $^\circ\text{C}$ for different times (0.5 , 1.5 , 3 , 4.5 , and 6 h) and dropped onto the surface of the modified MGCE. CA125 would automatically bind to the DNA on the electrode surface because of a specific selection of aptamer and antigen. The unbound CA125 was washed off with 20 mM PBS buffer (pH 7.4). The preparation steps of the label-free electrochemical biosensor were summarized in Fig. 1. To investigate the detection performance of the label-free electrochemical biosensor, differential pulse voltammetry (DPV) was used to explore the relationship between different concentrations of CA125 (5 – 125 U/mL) and peak currents under optimal detection conditions. (DPV parameters were set as follows: voltage range 0 – 0.6 V, amplitude 0.05 V, pulse width 0.06 s, sampling width 0.02 s, pulse period 0.5 s).

2.3. Preparation of artificial serum sample

To demonstrate the usability of the prepared aptasensor for the determination of CA125 in serum samples, an artificial serum sample was commercially obtained and was diluted 20 -fold with PBS buffer (20 mM, pH 7.4), which were spiked with different concentrations of CA125 (20 , 35 , 70 and 100 U/mL, within the range of the calibration plot). And finally, the spiked samples were analyzed by using the proposed aptasensor and also measured using the People's Hospital of Danyang Gold-standard Roche instrument as the reference value, and compared with the detection of DPV current peak in an artificial serum system to demonstrate the agreement of

our aptasensor with the Gold-standard Roche in terms of negative/positive judgment.

3. Results and discussion

3.1. Characterization of magnetic $\text{Mg}_{0.5}\text{Cu}_{0.5}\text{Fe}_2\text{O}_4$ nanoparticles

Fig. 2 showed the SEM morphology and the XRD pattern of the $\text{Mg}_{0.5}\text{Cu}_{0.5}\text{Fe}_2\text{O}_4$ NPs calcined at 800 $^\circ\text{C}$ for 2 h with absolute ethanol of 20 mL. From Fig. 2A, it could be seen that $\text{Mg}_{0.5}\text{Cu}_{0.5}\text{Fe}_2\text{O}_4$ NPs were well dispersed and relatively uniform with an average particle diameter of about 169.3 nm. The XRD patterns of $\text{Mg}_{0.5}\text{Cu}_{0.5}\text{Fe}_2\text{O}_4$ NPs and the standard PDF cards of MgFe_2O_4 (JCPDS No.36–0398) and CuFe_2O_4 (JCPDS No.77–0010) were shown in Fig. 2B. The diffraction peaks at 30.1° , 35.4° , 43.1° , 57.0° , and 62.6° indicated a composite state of MgFe_2O_4 and CuFe_2O_4 , which revealed that the $\text{Mg}_{0.5}\text{Cu}_{0.5}\text{Fe}_2\text{O}_4$ NPs had been successfully prepared.

The XRD patterns and the hysteresis loops of $\text{Mg}_{0.5}\text{Cu}_{0.5}\text{Fe}_2\text{O}_4$ NPs prepared at various temperatures with different volumes of absolute ethanol were revealed in Fig. 3. And according to the X-ray diffraction theory, when the crystalline grain size is less than 100 nm, the width of the diffraction peaks becomes significant with the decrease of grain size. Considering the effect of sample absorption and structure on the diffraction pattern, the average grain size was calculated by the Scherrer formula (Ahmad et al., 2022; Zhang et al., 2022b; Wabaidur et al., 2020):

$$D = 0.89\lambda/\beta \cos[\theta]$$

where D was the average grain size of $\text{Mg}_{0.5}\text{Cu}_{0.5}\text{Fe}_2\text{O}_4$ NPs (nm); β was the broadening of the diffraction peak measured at half maximum of the most intense peak; λ was the wavelength of Cu-K α radiation i.e. 1.5406 \AA , and θ was the Bragg diffraction angle.

As shown in Fig. 3A, when the volume of ethanol increased from 20 mL to 50 mL, the diffraction peaks of $\text{Mg}_{0.5}\text{Cu}_{0.5}\text{Fe}_2\text{O}_4$ NPs prepared at 400 $^\circ\text{C}$ for 2 h gradually narrowed and had a higher intensity, which could be clearly stated that the crystalline grain size gradually became larger. The reason might be that when the volume of ethanol was less than 50 mL, the increase of absolute ethanol prolonged the combustion time, so the grain size formed in the combustion process was gradually increased from 18.3 nm to 30.9 nm, and thereby the size of $\text{Mg}_{0.5}\text{Cu}_{0.5}\text{Fe}_2\text{O}_4$ NPs also increased. However, when the absolute ethanol increased to 100 mL, although the combustion time was also extended, the dispersion degree of absolute ethanol played a more significant role, thus the crystallinity decreased and the size was about 24.8 nm (Liu et al., 2021). The hysteresis loops were shown in Fig. 3B, the saturation magnetizations (M_s) grew stronger when the absolute ethanol increased from 20 mL to 40 mL. The M_s reached the maximum of about 44.5 emu/g when the absolute ethanol was 40 mL. However, the M_s weakened when the absolute ethanol was 50 mL, which was inconsistent with the results of XRD patterns in Fig. 3A, this might be due to a crystal defect. As demonstrated in Fig. 3C, with the calcination temperature increasing from 400 $^\circ\text{C}$ to 800 $^\circ\text{C}$, all diffraction peaks of $\text{Mg}_{0.5}\text{Cu}_{0.5}\text{Fe}_2\text{O}_4$ NPs calcined for 2 h with 20 mL absolute ethanol became narrower and sharper, and the grain

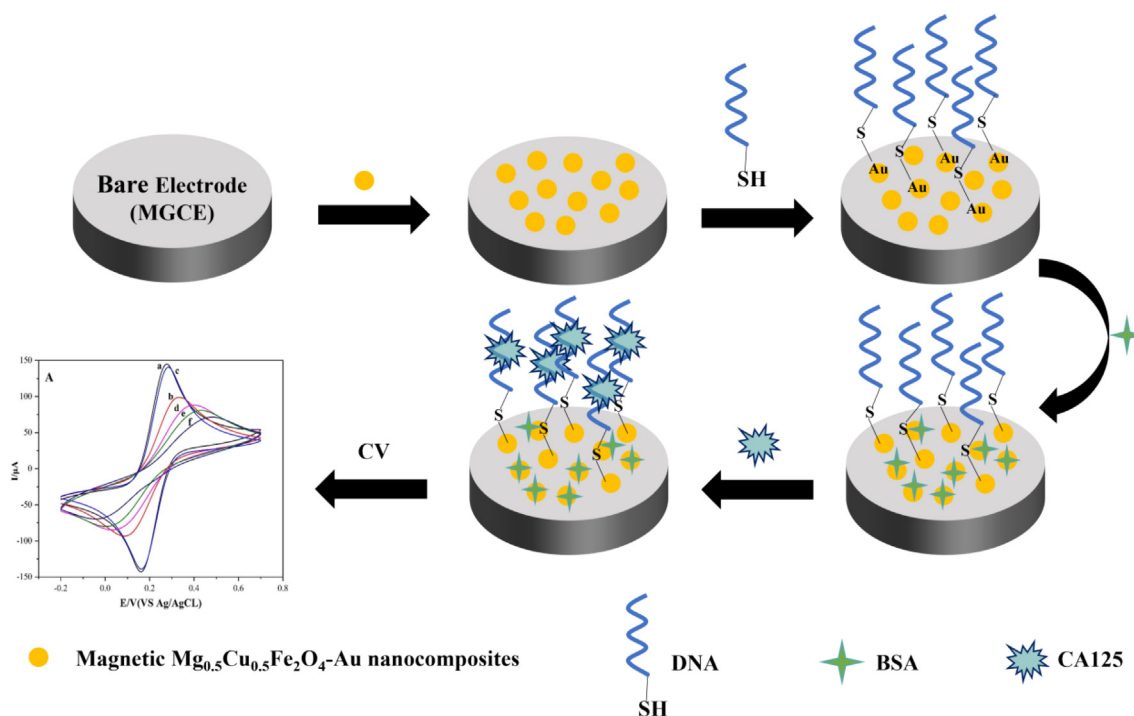


Fig. 1 Construction mechanism diagram of the label-free electrochemical biosensor based on magnetic $\text{Mg}_{0.5}\text{Cu}_{0.5}\text{Fe}_2\text{O}_4\text{-Au}$ nanocomposites.

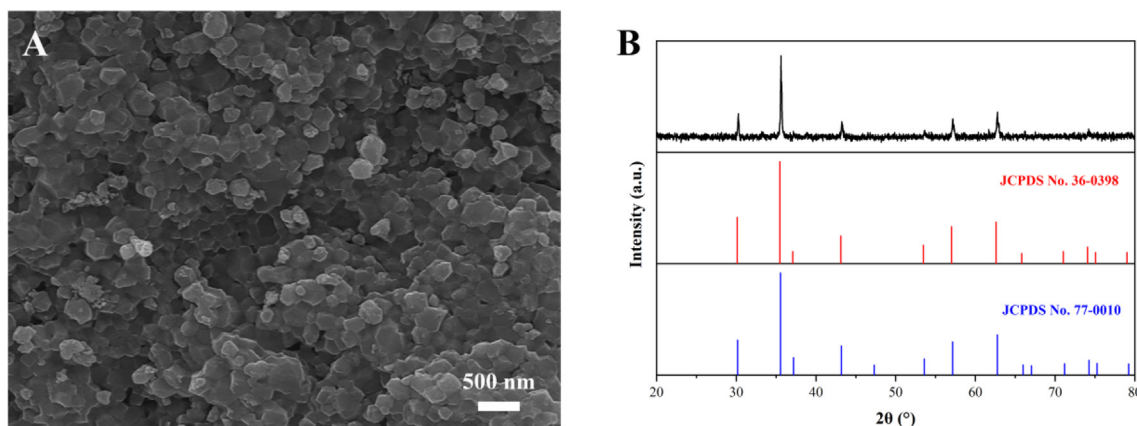


Fig. 2 SEM morphology (A), XRD pattern and standard XRD patterns (B) of magnetic $\text{Mg}_{0.5}\text{Cu}_{0.5}\text{Fe}_2\text{O}_4$ nanoparticles calcined at 800 °C for 2 h with 20 mL absolute ethanol.

size also gradually enlarged from 17.3 nm to 50.9 nm. And the same trend could be seen in Fig. 3D that the Ms increased obviously from 8.9 emu/g to 60.0 emu/g. The prepared $\text{Mg}_{0.5}\text{Cu}_{0.5}\text{Fe}_2\text{O}_4$ NPs exhibited typical superparamagnetic behavior. Thereby, the NPs could quickly self-assemble on the MGCE surface. After the test was completed, the NPs could be removed by rinsing the electrode to realize the reuse of the electrode, which would achieve low cost, simple and fast operation.

For reducing agglomeration of $\text{Mg}_{0.5}\text{Cu}_{0.5}\text{Fe}_2\text{O}_4$ NPs, the volume of absolute ethanol was selected as 20 mL. At the same time, for the more gold-modification sites and reducing the steric hindrance of aptamer DNA, the larger particle size should be selected, therefore, the $\text{Mg}_{0.5}\text{Cu}_{0.5}\text{Fe}_2\text{O}_4$ NPs prepared at 800 °C with suitable particle size and magnetic

strength were employed in subsequent experiments. In addition, compared with both ferrite Fe_3O_4 (Khalilzadeh et al., 2020; Xu et al., 2023) and $\text{Fe}_2\text{O}_3/\text{Fe}_3\text{O}_4$ (Ni et al., 2023; Zhang et al., 2023) nanomaterials, Fe_3O_4 was easy to agglomerate because of its strong magnetism. And $\text{Fe}_2\text{O}_3/\text{Fe}_3\text{O}_4$ would be oxidized and demagnetized because of prolonged storage. While $\text{Mg}_{0.5}\text{Cu}_{0.5}\text{Fe}_2\text{O}_4$ nanomaterials could overcome the disadvantages above.

3.2. Characterization of magnetic $\text{Mg}_{0.5}\text{Cu}_{0.5}\text{Fe}_2\text{O}_4\text{-Au}$ nanocomposites

$\text{Mg}_{0.5}\text{Cu}_{0.5}\text{Fe}_2\text{O}_4\text{-Au}$ NCs were detected by EDS as Fig. 4, the NCs contained Mg, Cu, Fe, O, and Au five elements, which

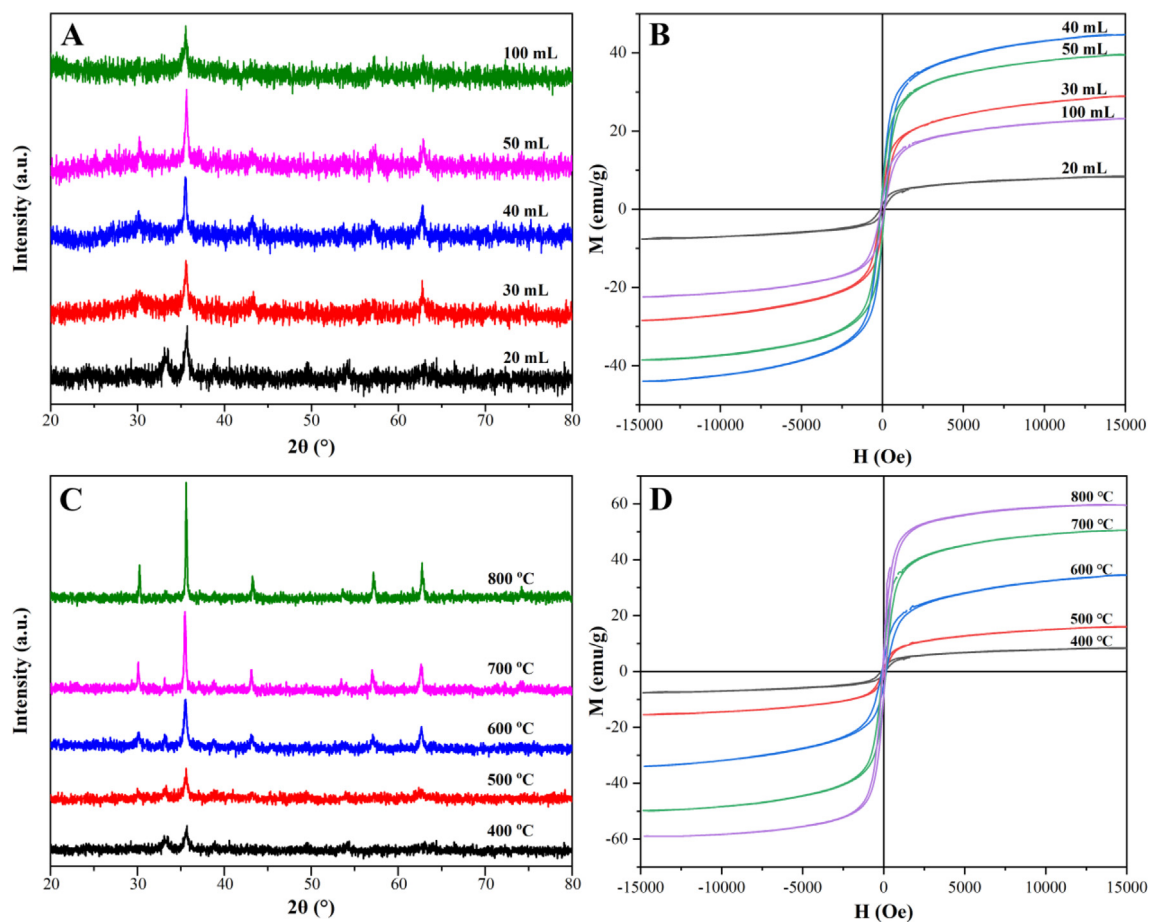


Fig. 3 XRD patterns (A, C) and the hysteresis loops (B, D) of magnetic $\text{Mg}_{0.5}\text{Cu}_{0.5}\text{Fe}_2\text{O}_4$ nanoparticles calcined at various temperatures with different volumes of absolute ethanol.

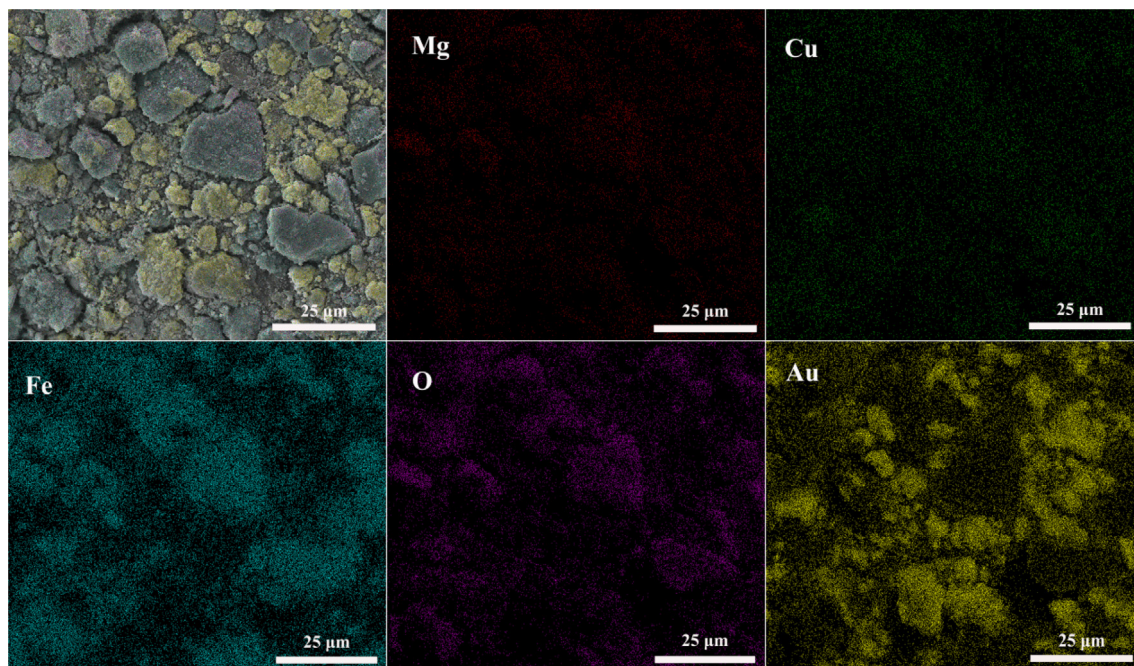


Fig. 4 EDS-Mapping of $\text{Mg}_{0.5}\text{Cu}_{0.5}\text{Fe}_2\text{O}_4$ -Au nanocomposites.

were distributed evenly. And Fig. 5 was the TEM image, EDS pattern, and XRD of the NPs and the NCs. The TEM image of $\text{Mg}_{0.5}\text{Cu}_{0.5}\text{Fe}_2\text{O}_4$ NPs shown in Fig. 5A, it could be seen that $\text{Mg}_{0.5}\text{Cu}_{0.5}\text{Fe}_2\text{O}_4$ NPs with an average particle size of about 169.3 nm had a smooth surface and no dark particles were attached. In Fig. 5B, uniformly distributed black spots with a particle size of about 7.2 nm could be seen loaded to the surface of $\text{Mg}_{0.5}\text{Cu}_{0.5}\text{Fe}_2\text{O}_4$ large nanoparticles. In addition, the EDS pattern of Fig. 5C and the XRD pattern of Fig. 5D also confirmed the successful adhesion of Au nanoparticles. From Fig. 5C, the atomic percentages of Mg, Cu, Fe, O, and Au were 2.57%, 6.46%, 26.55%, 22.42%, and 42.00% respectively. And from Fig. 5D the diffraction peaks of Au were located at 38.3° , 44.6° , 64.7° , and 77.5° , indicating that $\text{Mg}_{0.5}\text{Cu}_{0.5}\text{Fe}_2\text{O}_4$ -Au NCs have been successfully prepared.

3.3. Fabrication of label-free biosensor and electrochemical characterization

The fabrication process of the CA125-specific biosensor was monitored in each MGCE modification step by CV and EIS. For this, $[\text{Fe}(\text{CN})_6]^{3-/4-}$ (5 mM), which contained 0.1 M of KCl, was used as a redox probe for all electrochemical measurements. Fig. 6 displayed the CV and EIS measurements of bare MGCE, MGCE/ $\text{Mg}_{0.5}\text{Cu}_{0.5}\text{Fe}_2\text{O}_4$, MGCE/ $\text{Mg}_{0.5}\text{Cu}_{0.5}\text{Fe}_2\text{O}_4$ -Au, MGCE/ $\text{Mg}_{0.5}\text{Cu}_{0.5}\text{Fe}_2\text{O}_4$ -Au/DNA-aptamer, MGCE/ $\text{Mg}_{0.5}\text{Cu}_{0.5}\text{Fe}_2\text{O}_4$ -Au/DNA-aptamer/BSA, and MGCE/ $\text{Mg}_{0.5}\text{Cu}_{0.5}\text{Fe}_2\text{O}_4$ -Au/DNA-aptamer/BSA/CA125. It could be seen that the bare MGCE had a reversible redox peak from Fig. 6A(a). After $\text{Mg}_{0.5}\text{Cu}_{0.5}\text{Fe}_2\text{O}_4$ NPs modified the MGCE surface, the $[\text{Fe}(\text{CN})_6]^{3-/4-}$ redox current magnitude decreased significantly (Fig. 6A(b)), because the low electrical conductivity of $\text{Mg}_{0.5}\text{Cu}_{0.5}\text{Fe}_2\text{O}_4$ NPs and the steric hindrance effect made it difficult for the redox probe $[\text{Fe}(\text{CN})_6]^{3-/4-}$ to reach the electrode surface. After $\text{Mg}_{0.5}\text{Cu}_{0.5}\text{Fe}_2\text{O}_4$ NPs were modified with Au nanoparticles, the redox current increased significantly (Fig. 6A(c)). Because Au had more free electrons with high conductivity, which could improve the electron transfer efficiency and even amplify the redox current (Weng et al., 2020). After the TCEP-reduced aptamer DNA disulfide was fixed on the surface of the material, the redox current decreased (Fig. 6A(d)), which was due to the electrostatic repulsion between the negatively charged DNA phosphate skeleton and the redox probe, and its steric hindrance was large (Zhang et al., 2018). The subsequent addition of the blocker BSA to prevent non-specific site interference also reduced the current signal (Fig. 6A(e)) due to the increased steric hindrance (Öndeş et al., 2021). The current was further reduced by the addition of the CA125 antigen (Fig. 6A(f)) because CA125 had a large steric hindrance, which could hinder the transmission of signals.

EIS measurements were carried out to investigate the electron transfer properties of the prepared electrodes. The inset showed the equivalent circuit simulation diagram of MGCE/ $\text{Mg}_{0.5}\text{Cu}_{0.5}\text{Fe}_2\text{O}_4$ -Au/DNA-aptamer/BSA/CA125 (Bard et al., 1980; Largeot et al., 2008; De Levie 1963; Taberna et al., 2003). As demonstrated in Fig. 6B, the results consisting of CV plots were revealed. The impedance of the modified MGCE with $\text{Mg}_{0.5}\text{Cu}_{0.5}\text{Fe}_2\text{O}_4$ NPs (Fig. 6B(b)) was relatively higher than that of the bare MGCE (Fig. 6B(a)). This result

could be explained by the fact that the $\text{Mg}_{0.5}\text{Cu}_{0.5}\text{Fe}_2\text{O}_4$ NPs were a type of insulator, which did not allow electron transfer and showed resistance. Additionally, the semicircle diameter of MGCE/ $\text{Mg}_{0.5}\text{Cu}_{0.5}\text{Fe}_2\text{O}_4$ -Au (Fig. 6B(c)) was much smaller than that of MGCE/ $\text{Mg}_{0.5}\text{Cu}_{0.5}\text{Fe}_2\text{O}_4$ (Fig. 6B(b)), which was caused by the Au particles amplifying the current. CV measurements also obtained the same results. The semicircle diameter of MGCE/ $\text{Mg}_{0.5}\text{Cu}_{0.5}\text{Fe}_2\text{O}_4$ -Au/DNA-aptamer (Fig. 6B(d)), MGCE/ $\text{Mg}_{0.5}\text{Cu}_{0.5}\text{Fe}_2\text{O}_4$ -Au/DNA-aptamer/BSA (Fig. 6B(e)), MGCE/ $\text{Mg}_{0.5}\text{Cu}_{0.5}\text{Fe}_2\text{O}_4$ -Au/DNA-aptamer/BSA/CA125 (Fig. 6B(f)) increased in turn as expected, which was also consistent with the results of CV measurements. It showed that MGCE/ $\text{Mg}_{0.5}\text{Cu}_{0.5}\text{Fe}_2\text{O}_4$ -Au/DNA-aptamer/BSA/CA125 label-free electrochemical biosensor was successfully fabricated. The above results proved that the design of the electrochemical aptamer sensor was feasible.

3.4. Parameter optimization of label-free electrochemical biosensor

The DPV measurement was carried out to detect three key experimental conditions. The optimal conditions were obtained from Fig. 7.

The effect of $\text{Mg}_{0.5}\text{Cu}_{0.5}\text{Fe}_2\text{O}_4$ -Au NCs concentration on DPV was shown in Fig. 7A, the maximum current was 107.5 μA when the concentration of $\text{Mg}_{0.5}\text{Cu}_{0.5}\text{Fe}_2\text{O}_4$ -Au NCs reached 15 mg/mL. This could be explained by the poor conductivity, namely, the insufficient amount of the $\text{Mg}_{0.5}\text{Cu}_{0.5}\text{Fe}_2\text{O}_4$ -Au NCs was not enough to cause a large electrical signal change when the concentration was lower than 15 mg/mL. While the concentration was higher than 15 mg/mL, the excessive steric hindrance made the $[\text{Fe}(\text{CN})_6]^{3-/4-}$ probe difficult to reach the electrode surface and the current decreased. Therefore, the optimal concentration of the NCs $\text{Mg}_{0.5}\text{Cu}_{0.5}\text{Fe}_2\text{O}_4$ -Au was selected as 15 mg/mL.

The effect of DNA-aptamer concentration on DPV was revealed in Fig. 7B, the steric hindrance of DNA gradually enlarged with the increase of DNA concentration (4, 6, 8, 10, and 12 μM). In addition, the repulsive force between the negative charge of the DNA phosphate backbone and $[\text{Fe}(\text{CN})_6]^{3-/4-}$ probe gradually increased, also resulting in the gradual decrease of the current. When the concentration of DNA was higher than 10 μM , the current was stable at 26.5 μA . At this point, the amount of DNA attached to the electrode surface had reached a saturation state, and the increase in DNA concentration no longer caused much change in the current. Therefore, 10 μM was used as the optimal concentration of DNA-aptamer.

The effect of CA125 incubation time on DPV was displayed in Fig. 7C, the peak current gradually decreased and finally tended to be stable after 3 h. The reason why it took as long as 3 h of bonding time might be due to the isoelectric point (pI) of the CA125 protein of 6.2 and the pH of 7.4 in the human body, which was also 7.4 in the testing environment. In this case, the protein was negatively charged, resulting in electrostatic repulsion from the negatively charged DNA-aptamer phosphate skeleton, and the hydrogen bonding between the protein and DNA might be hindered, resulting in prolonged incubation time. Thus, 3 h was used to be the optimal incubation time.

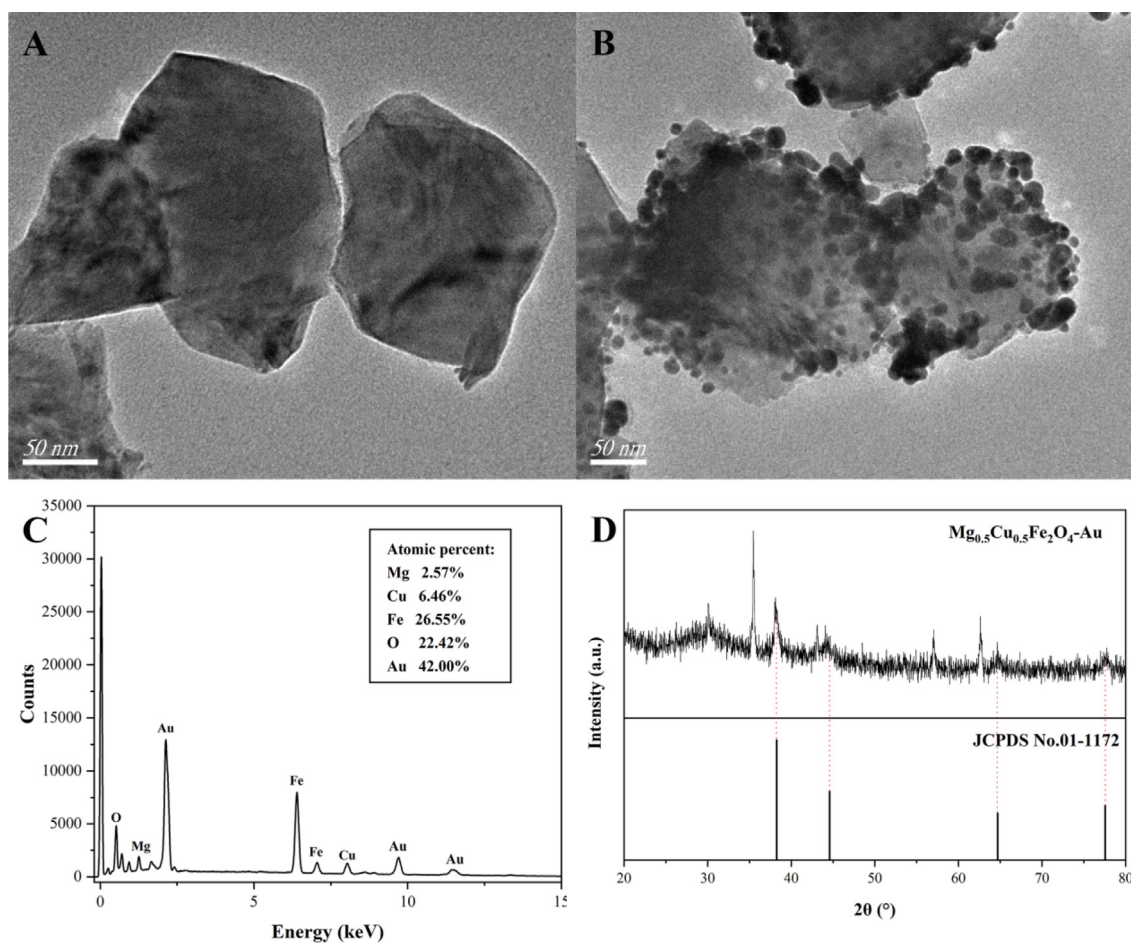


Fig. 5 TEM image of $\text{Mg}_{0.5}\text{Cu}_{0.5}\text{Fe}_2\text{O}_4$ nanoparticles (A); TEM image (B), EDS pattern (C), and XRD (D) of $\text{Mg}_{0.5}\text{Cu}_{0.5}\text{Fe}_2\text{O}_4$ -Au nanocomposites.

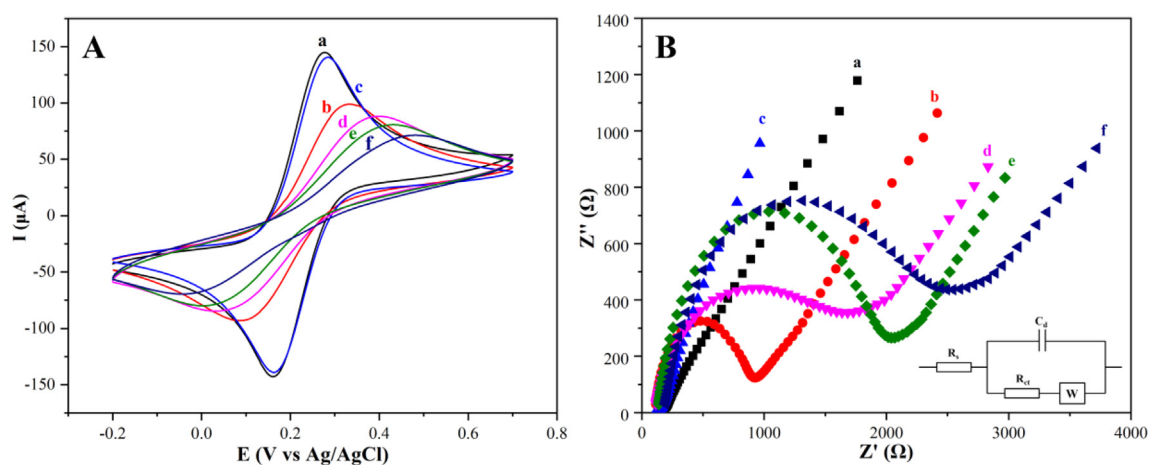


Fig. 6 CV profiles (A), Nyquist diagram (B), and the circuit simulation graph (inset) of bare MGCE (a), MGCE/ $\text{Mg}_{0.5}\text{Cu}_{0.5}\text{Fe}_2\text{O}_4$ (b), MGCE/ $\text{Mg}_{0.5}\text{Cu}_{0.5}\text{Fe}_2\text{O}_4$ -Au (c), MGCE/ $\text{Mg}_{0.5}\text{Cu}_{0.5}\text{Fe}_2\text{O}_4$ -Au/DNA-aptamer (d), MGCE/ $\text{Mg}_{0.5}\text{Cu}_{0.5}\text{Fe}_2\text{O}_4$ -Au/DNA-aptamer/BSA (e), MGCE/ $\text{Mg}_{0.5}\text{Cu}_{0.5}\text{Fe}_2\text{O}_4$ -Au/DNA-aptamer/BSA/CA125 (f) in 0.1 M of KCl containing 5 mM $[\text{Fe}(\text{CN})_6]^{3-/4-}$ at 25 °C.

3.5. Detection performance of the label-free electrochemical biosensor

To test the detection performance, DPV responses of the MGCE/ $\text{Mg}_{0.5}\text{Cu}_{0.5}\text{Fe}_2\text{O}_4$ -Au/DNA-aptamer/BSA electro-

chemical biosensor with the increase of CA125 concentration (5–125 U/mL) were investigated, the clinical levels of ovarian cancer patients were covered, and the obtained results were summarized in Fig. 8A. It could be noted that the DPV peak current decreased with the increase of CA125 concentration,

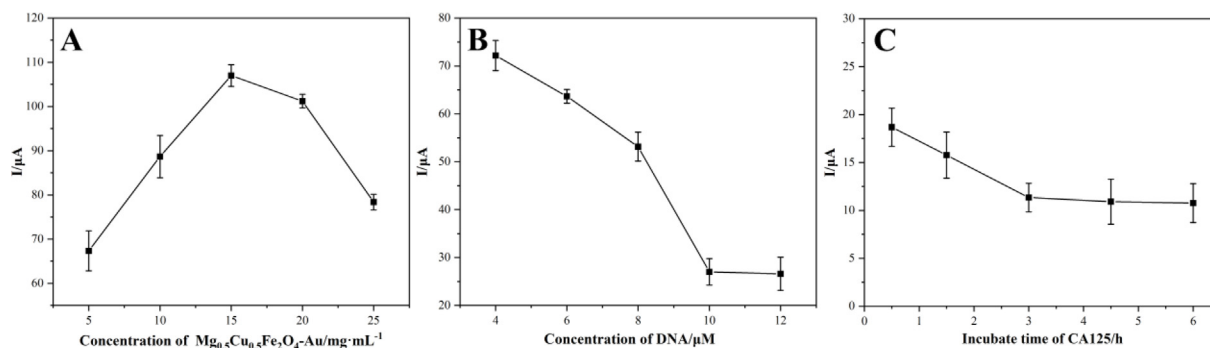


Fig. 7 DPV response diagrams of $\text{Mg}_{0.5}\text{Cu}_{0.5}\text{Fe}_2\text{O}_4\text{-Au}$ NCs concentration (A), DNA concentration (B), and the incubating time of CA125 (C) in 0.1 M of KCl containing 5 mM $[\text{Fe}(\text{CN})_6]^{3-/4-}$ at 25 °C.

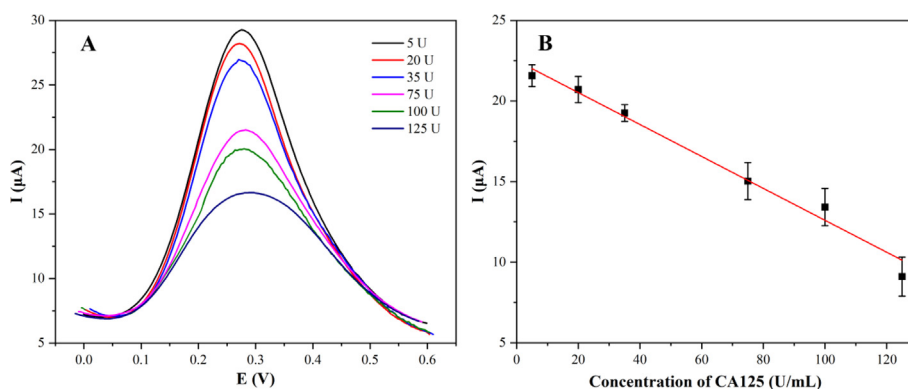


Fig. 8 DPVs current responses of CA125 at six concentrations (5 U/mL, 20 U/mL, 35 U/mL, 75 U/mL, 100 U/mL, and 125 U/mL) (A), calibration graph of the response current vs different CA125 antigen concentrations (B) in 0.1 M of KCl containing 5 mM $[\text{Fe}(\text{CN})_6]^{3-/4-}$ under optimal experiment conditions at 25 °C.

under the optimal experimental conditions. These results were in line with those obtained in DPV-based biosensor studies reported in the literature (Biswas et al., 2021), which demonstrated that the peak current decreased with the increase in antigen concentration. Due to the steric hindrance and non-conductivity of the protein, the electron transfer was reduced and the current signal was reduced as well. The linear relationship between peak currents and the concentration of tumor marker CA125 was shown in Fig. 8B, and the linear regression equation was $I(\mu\text{A}) = -0.0990C (\text{U/mL}) + 22.5009$ ($R^2 = 0.9844$), the limit of detection (LOD) and the limit of quantification (LOQ) were calculated as 4.4 U/mL ($S/N = 3$) and 14.8 U/mL ($S/N = 10$), respectively. LOD was calculated by three times the standard deviation of the blank divided by the slope of the calibration curve. Whereas, the 10-fold difference from LOD was described as LOQ (Öndeş et al., 2021). Since the pathophysiological level of CA125 did not exceed 35 U/mL in normal human serum (Al-Ogaidi et al., 2014), this presented biosensor could be used to detect ovarian cancer for medicinal purposes and could be also used as a normality indicator. In addition, a comparison of the biosensor in this study with the previous reports about various biosensor for the detection of CA125 protein was listed in Table 1. The quantitative range and LOD of our novelty DNA-aptamer biosensor display a good advantage over other reported measurements.

3.6. Reproducibility, selectivity, and stability of the biosensor

Selectivity, stability, and reproducibility were necessary factors to evaluate the efficiency of biosensors. Therefore, interferents Human mucin 1 (MUC1), Immunoglobulin E (IgE), Human epidermal growth factor receptor 2 (HER2), and Albumin (Alb) were employed to verify the selectivity. The concentration of all the above-mentioned interferents was set at 1000 U/mL, while the concentration of CA125 was set at 100 U/mL. Fig. 9A showed that electron transfer was hindered due to the steric hindrance and non-conductivity of the CA125 protein, which made the electrical signals of the target protein CA125 weaker than those for other interfering proteins. However, the electrical signals, the interference protein mixed with the target protein CA125 (Mix), were close to that of the target protein of CA125, which also indicated that the proposed biosensor had higher specificity for CA125. To examine the reproducibility of the fabricated biosensor, the DPV measurement was carried out to detect five individual aptasensors incubated under optimal reaction conditions. The mean relative standard deviation (RSD) was 2.53% ($n = 5$), which demonstrated that the reproducibility of the biosensor was at an acceptable level. In order to investigate the stability of the biosensor prepared under the optimal reaction conditions, the biosensors were stored at 4 °C for 14 days while CA125 was measured every two days at a concentration of 50 U/

Table 1 Comparison of the proposed biosensor with other various reports for the detection of CA125 protein.

Materials	Linear Range	LOD
Aptasensor based on AuNPs/GaN (Hu et al., 2020)	1–100 U/mL	0.3 U/mL
Immunosensor based on SPEs/poly(3-HPA) (De Castro et al., 2020)	5–80 U/mL	1.45 U/mL
Immunosensor based on GNs (Torati et al., 2017)	10–100 U/mL	5.5 U/mL
Immunosensor based on DGN (Kumar et al., 2018)	20–100 U/mL	3.4 U/mL
Aptasensor based on SPEs/GNs (Chen et al., 2019)	0.05–50 ng/mL	5.0 pg/mL
Immunosensor based on carbon nanofiber (Wu et al., 2007)	2–75 U/mL	1.8 U/mL
Immunosensor based on SPE/AuNPs (Ravalli et al., 2013)	0–100 U/mL	6.7 U/mL
Immunosensor based on thin-film IDA (Ravalli et al., 2016)	0–100 U/mL	7.0 U/mL
Mg _{0.5} Cu _{0.5} Fe ₂ O ₄ -Au NCs modified MGCE (This work)	5–125 U/mL	4.4 U/mL

*Gallium nitride (GaN); Screen-printed electrodes (SPEs); 3-hydroxyphenylacetic acid (3-HPA); Gold nanostructures (GNs); Dual gold nanostructure (DGN); interdigitated gold array microelectrodes (IDA).

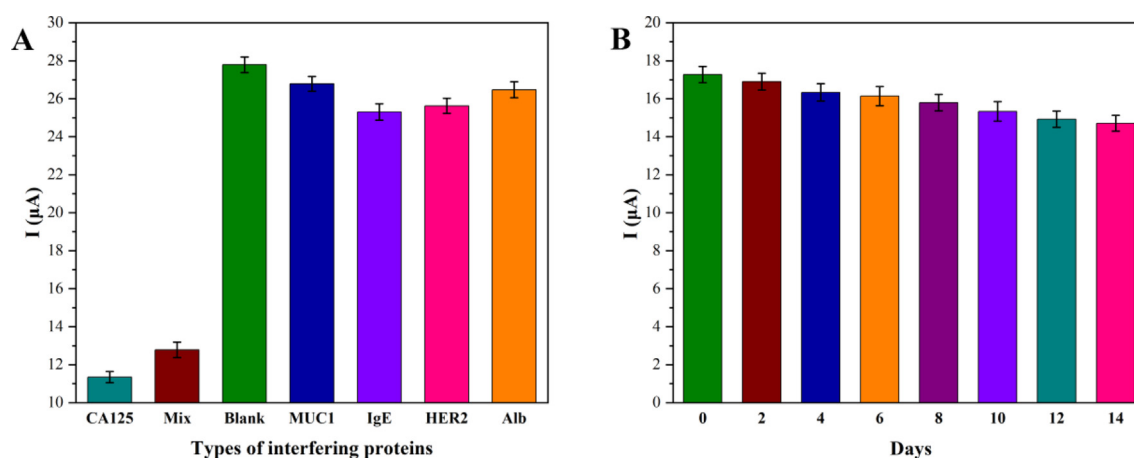


Fig. 9 Selectivity assessment of the electrochemical aptasensor with CA125 (100 U/mL), MUC1 (1000 U/mL), IgE (1000 U/mL), HER2 (1000 U/mL), Alb (1000 U/mL) (A), stability (B) of Mg_{0.5}Cu_{0.5}Fe₂O₄-Au/DNA modified biosensor at 4 °C. (n = 5) *MUC1 (Human mucin 1); IgE (Immunoglobulin E); HER2 (Human epidermal growth factor receptor 2); Alb (Albumin).

Table 2 Determination of different CA125 protein concentrations in spiked human serum samples (n = 3).

Spiked (U/mL)	Gold-standard Roche instrument		Electrochemical aptasensor	
	Measured value (U/mL)	Recovery (%)	Mean ± RSD (U/mL)	Recovery (%)
20	19.51	97.55	18.93 ± 0.0465	94.65
35	32.49	92.83	35.43 ± 0.0126	101.23
70	70.33	100.47	66.31 ± 0.0266	94.73
100	100.13	100.13	100.71 ± 0.0440	100.71

mL. The experimental results were shown in Fig. 9B, the prepared aptasensor remained at 85.14% of the initial response after two weeks. These results demonstrated that the designed biosensor had great reproducibility, selectivity, and storage stability.

3.7. Detection of CA125 in spiked serum

To verify the practical ability of detecting CA125 of the bio-platform, the spiked serum samples were tested using DPV. Healthy human serum was 20-fold diluted by 20 mM PBS (pH 7.4) and spiked with CA125 using a standard addition method. As listed in Table 2, the data showed that the recovery

rates of real serum samples were 94.65–101.71%, with the RSDs ranging from 1.26 to 4.65%. The results were comparable to the Gold-standard Roche instrument test, which demonstrated the dependability and accuracy for quantitative analysis of CA125 in human serum samples for early diagnosis of ovarian cancer. Therefore, the prepared bio-platform was a promising tool for detecting CA125 in clinical samples due to its strong selectivity, excellent anti-interference ability, and signal amplification effect of Mg_{0.5}Cu_{0.5}Fe₂O₄-Au. It was expected that the constructed biosensor would have broad application prospects and potential in the early clinical diagnosis of ovarian cancer.

4. Conclusions

Here, a label-free electrochemical aptasensor was successfully constructed for the sensitive detection of tumor marker CA125 based on magnetic $Mg_{0.5}Cu_{0.5}Fe_2O_4$ -Au NCs. The as-constructed electrochemical DNA-aptamer biosensor had a large linear range of 5–125 U/mL and a low LOD of 4.4 U/mL ($S/N = 3$). While, the biosensor revealed good specificity, reproducibility ($RSD = 2.53\%$), and reasonable storage stability. After storing the biosensor at 4 °C for 14 days, the signal remained at 85.14% of the original signal. Additionally, this aptasensor was successfully used for the determination of CA125 in artificial serum samples, with recovery rates of 94.65–101.71%. Compared with Gold-standard Roche instrument detection in an artificial serum system, the recovery rates were 92.83–100.13%, which demonstrated the feasibility of the aptasensor. Thus, it had broad application prospects and potential in the early clinical detection of ovarian cancer. Also, this aptasensor platform showed potential for possible POC applications.

CRedit authorship contribution statement

Yao Yue: Conceptualization, Writing – original draft, Methodology, Formal analysis, Data curation. **Xiu Chen:** Funding acquisition, Investigation, Visualization. **Jie Wang:** Software, Data curation. **Mingyi Ma:** Resources, Writing – review & editing. **Aolin He:** Funding acquisition, Visualization, Investigation. **Ruijiang Liu:** Conceptualization, Project administration, Formal analysis, Writing – review & editing, Supervision.

Declaration of Competing Interest

The authors declare that they have no known competing financial interests or personal relationships that could have appeared to influence the work reported in this paper.

Acknowledgments

This work was supported by the Jiangsu Provincial Postgraduate Scientific Practice and Innovation Project (Grant No. SJCX21_1722) and the Science and Technology Innovation Project of CHN Energy (Grant No. GJNY-20-109).

References

- Ahmad, Y., Raina, B., Thakur, S., Bamzai, K.K., 2022. Magnesium and yttrium doped superparamagnetic manganese ferrite nanoparticles for magnetic and microwave applications. *J. Magn. Mater.* 552, 169178.
- Ahmadi, M., Ghoorchian, A., Dashtian, K., Kamalabadi, M., Madrakian, T., Afkhami, A., 2021. Application of magnetic nanomaterials in electroanalytical methods: A review. *Talanta* 225, 121974.
- Al-Ogaidi, I., Gou, H., Aguilar, Z.P., Guo, S., Melconian, A.K., Al-Kazaz, A.K.A., Meng, F., Wu, N., 2014. Detection of the ovarian cancer biomarker CA-125 using chemiluminescence resonance energy transfer to graphene quantum dots. *Chem. Commun.* 50, 1344–1346.
- Asghar, K., Qasim, M., Dharmapuri, G., et al, 2020. Thermoresponsive polymer gated and superparamagnetic nanoparticle embedded hollow mesoporous silica nanoparticles as smart multifunctional nanocarrier for targeted and controlled delivery of doxorubicin. *Nanotechnology* 31, 455604.
- Bard, A.J., Faulkner, L.R., Leddy, J., Zoski, C.G., 1980. Electrochemical methods: fundamentals and applications. *Mater. Sci.*
- Bi, R., Ma, X., Miao, K., Ma, P., Wang, Q., 2023. Enzymatic biosensor based on dendritic gold nanostructure and enzyme precipitation coating for glucose sensing and detection. *Enzyme Microb. Tech.* 162, 110132.
- Biswas, S., Lan, Q., Xie, Y., Sun, X., Wang, Y., 2021. Label-free electrochemical immunosensor for ultrasensitive detection of carbohydrate antigen 125 based on antibody-immobilized biocompatible MOF-808/CNT. *ACS. Appl. Mater. Inter.* 13, 3295–3302.
- Chen, J.S., Hu, W.B., Wei, J., Yu, F., Wu, L., Wang, C.M., Wang, W., Zuo, S.Y., Shang, B., Chen, Q.H., 2019. An electrochemical aptasensing platform for carbohydrate antigen 125 based on the use of flower-like gold nanostructures and target-triggered strand displacement amplification. *Microchem. Acta* 186, 388–395.
- De Castro, A.C.H., Alves, L.M., Siquieroli, A.C.S., Madurro, J.M., Brito-Madurro, A.G., 2020. Label-free electrochemical immunosensor for detection of oncomarker CA125 in serum. *Microchem. J.* 155, 33–84.
- De Levie, R., 1963. On porous electrodes in electrolyte solutions: I. Capacitance effects. *Electrochim. Acta* 8, 751–780.
- Ebrahimi, N., Raoof, J.B., Ojani, R., Ebrahimi, M., 2022. Designing a novel DNA-based electrochemical biosensor to determine of Ba^{2+} ions both selectively and sensitively. *Anal. Biochem.* 642, 114563.
- Franier, B., Thompson, M., 2019. Early stage detection and screening of ovarian cancer: A research opportunity and significant challenge for biosensor technology. *Biosens. Bioelectron.* 135, 71–81.
- Giamougiannis, P., Martin-Hirsch, P.L., Martin, F.L., 2021. The evolving role of MUC16 (CA125) in the transformation of ovarian cells and the progression of neoplasia. *Carcinogenesis* 42, 327–343.
- Hu, D.L., Liang, H.F., Wang, X.Y., Luo, F., Qiu, B., Lin, Z.Y., Wang, J., 2020. Highly sensitive and selective photoelectrochemical aptasensor for cancer biomarker CA125 based on AuNPs/GaN Schottky junction. *Anal. Chem.* 92, 10114–10120.
- Jin, H., Dong, J., Qi, X., et al, 2023. A label-free impedance-based electrochemical sensor based on self-assembled dendritic DNA nanostructures for Pb^{2+} detection. *Bioelectrochemistry* 149, 108312.
- Khalilzadeh, M.A., Tajik, S., Beitollahi, H., Venditti, R.A., 2020. Green synthesis of magnetic nanocomposite with iron oxide deposited on cellulose nanocrystals with copper ($Fe_3O_4@CNC/Cu$): Investigation of catalytic activity for the development of a venlafaxine electrochemical sensor. *Ind. Eng. Chem. Res.* 59, 4219–4228.
- Kumar, N., Sharma, S., Nara, S., 2018. Dual gold nanostructure-based electrochemical immunosensor for CA125 detection. *Appl. Nanosci.* 8, 1843–1853.
- Lai, H., Guo, Y., Tian, L., et al, 2022. Protein panel of serum-derived small extracellular vesicles for the screening and diagnosis of epithelial ovarian cancer. *Cancers* 14, 3719.
- Largeot, C., Portet, C., Chmiola, J., Taberna, P.L., Gogotsi, Y., Simon, P., 2008. Relation between the ion size and pore size for an electric double-layer capacitor. *J. Am. Chem. Soc.* 130, 2730–2731.
- Li, X., Jia, M., Yu, L., et al, 2023. An ultrasensitive label-free biosensor based on aptamer functionalized two-dimensional photonic crystal for kanamycin detection in milk. *Food Chem.* 402, 134239.
- Liu, Y., Li, Y., Rao, Z.K., et al, 2019. Physicochemical properties and paclitaxel release behaviors of dual-stimuli responsive copolymer-magnetite superparamagnetic nanocomposites. *Nanotechnology* 30, 105602.
- Liu, R., Pan, S., Liu, M., Huang, W., Lv, Z., He, A., 2021. A label-free electrochemical biosensor with magnetically induced self-assembly for the detection of the CYP2C9*3 gene. *Appl. Surf. Sci.* 537, 147868.
- Liu, R., Rong, G., Liu, Y., Huang, W., He, D., Lu, R., 2021. Delivery of apigenin-loaded magnetic $Fe_2O_3/Fe_3O_4@mSiO_2$ nanocomposites to A549 cells and their antitumor mechanism. *Mat. Sci. Eng. C-Mater.* 120, 111719.

- Liu, Z., Wang, J., Cui, C., Zheng, L., Hu, L., 2023. Introducing AgNPs-VB₂ composites as the dual signal quenching of CeO₂-AuNPs-g-CNQDs hybrids for ultrasensitive “on-off” electrochemiluminescence immunosensing of prostate specific antigen. *Talanta* 252, 123886.
- Low, S.S., Ji, D., Chai, W.S., et al, 2021. Recent progress in nanomaterials modified electrochemical biosensors for the detection of microRNA. *Micromachines* 12, 1409.
- Malekzad, H., Hasanzadeh, M., Shadjou, N., Jouyban, A., 2017. Highly sensitive immunosensing of prostate specific antigen using poly cysteine capped by graphene quantum dots and gold nanoparticle: A novel signal amplification strategy. *Int. J. Biol. Macromol.* 105, 522–532.
- Nash, Z., Menon, U., 2020. Ovarian cancer screening: Current status and future directions. *Best Pract. Res. Cl. Ob.* 65, 32–45.
- Negahdary, M., Angnes, L., 2022. Electrochemical aptamer-based nanobiosensors for diagnosing Alzheimer’s disease: A review. *Mat. Sci. Eng. C-Mater.* 135, 112689.
- Ni, Y., Ouyang, H.Z., Yu, L.L., Ling, C., Zhu, Z.Y., He, A.L., Liu, R. J., 2022. Label-free electrochemical aptasensor based on magnetic α -Fe₂O₃/Fe₃O₄ heterogeneous hollow nanorods for the detection of cancer antigen 125. *Bioelectrochemistry* 148, 108255.
- Ni, Y., Chen, X., Ling, C., Zhu, Z.Y., Yue, Y., Wang, J., He, A.L., Liu, R.J., 2023. Electrochemical peptide nucleic acid functionalized alpha-Fe₂O₃/Fe₃O₄ nanosheets for detection of CYP2C19*2 gene. *Microchim. Acta* 190, 1436–5073.
- Öndeş, B., Evli, S., Uygun, M., Uygun, D.A., 2021. Boron nitride nanosheet modified label-free electrochemical immunosensor for cancer antigen 125 detection. *Biosens. Bioelectron.* 191, 113454.
- Peng, Y., Lu, B., Deng, Y., Yang, N., Li, G., 2022. A dual-recognition-controlled electrochemical biosensor for accurate and sensitive detection of specific circulating tumor cells. *Biosens. Bioelectron.* 201, 113973.
- Pumera, M., Sanchez, S., Ichinose, I., Tang, J., 2007. Electrochemical nanobiosensors. *Sensor. Actuat. B-Chem.* 123, 1195–1205.
- Ravalli, A., Dos Santos, G.P., Ferroni, M., Faglia, G., Yamanaka, H., Marrazza, G., 2013. New label free CA125 detection based on gold nanostructured screen-printed electrode. *Sensor. Actuat. B-Chem.* 179, 194–200.
- Ravalli, A., Lozzi, L., Marrazza, G., 2016. Micro-flow immunosensor based on thin-film interdigitated gold array microelectrodes for cancer biomarker detection. *Curr. Drug. Deliv.* 13, 400–408.
- Reverté, L., Simón, B.P., Campàs, M., 2016. New advances in electrochemical biosensors for the detection of toxins: Nanomaterials, magnetic beads and microfluidics systems. A review. *Anal. Chim. Acta* 908, 8–21.
- Sadasivam, M., Sakthivel, A., Nagesh, N., Hansda, S., Veerapandian, M., Alwarappan, S., Manickam, P., 2020. Magnetic bead-amplified voltammetric detection for carbohydrate antigen 125 with enzyme labels using aptamer-antigen-antibody sandwiched assay. *Sensor. Actuat. B-Chem.* 321, 127985.
- Sun, C., Shen, Y., Zhang, Y., Du, Y., Peng, Y., Xie, Q., 2022. Sandwich photoelectrochemical biosensing of concanavalin A based on CdS/AuNPs/NiO Z-scheme heterojunction and lectin-sugar binding. *Talanta* 253, 123882.
- Sung, H., Ferlay, J., Siegel, R.L., et al, 2021. Global cancer statistics 2020: GLOBOCAN estimates of incidence and mortality worldwide for 36 cancers in 185 countries. *CA-Cancer J. Clin.* 71, 209–249.
- Taberna, P.L., Simon, P., Fauvarque, J.F., 2003. Electrochemical characteristics and impedance spectroscopy studies of carbon-carbon supercapacitors. *J. Electrochem. Soc.* 150, A292–A300.
- Torati, S.R., Kasturi, K.C.S.B., Lim, B., Kim, C.G., 2017. Hierarchical gold nanostructures modified electrode for electrochemical detection of cancer antigen CA125. *Sensor. Actuat. B-Chem.* 243, 64–71.
- Wabaidur, S.M., Khan, M.A., Siddiqui, M.R., Otero, M., Jeon, B.H., Alothman, Z.A., Hakami, A.A.H., 2020. Oxygenated functionalities enriched MWCNTs decorated with silica coated spinel ferrite-A nanocomposite for potentially rapid and efficient de-colorization of aquatic environment. *J. Mol. Liq.* 317, 113916.
- Weng, C., Li, X., Lu, Q., Yang, W., Wang, J., Yan, X., Li, B., Sakran, M., Hong, J., Zhu, W., Zhou, X., 2020. A label-free electrochemical biosensor based on magnetic biocomposites with DNAzyme and hybridization chain reaction dual signal amplification for the determination of Pb²⁺. *Microchim. Acta* 187, 575.
- White, B., Patterson, M., Karnwal, S., Brooks, C.L., 2022. Crystal structure of a human MUC16 SEA domain reveals insight into the nature of the CA125 tumor marker. *Proteins* 90, 1210–1218.
- Wu, L.N., Yan, F., Ju, H.X., 2007. An amperometric immunosensor for separation-free immunoassay of CA125 based on its covalent immobilization coupled with thionine on carbon nanofiber. *J. Immunol. Methods* 322, 12–19.
- Xu, Q.Q., Luo, L., Liu, Z.G., Guo, Z., Huang, X.J., 2023. Highly sensitive and selective serotonin (5-HT) electrochemical sensor based on ultrafine Fe₃O₄ nanoparticles anchored on carbon spheres. *Biosens. Bioelectron.* 222, 114990.
- Yu, L., Liu, M., Zhang, Y., Ni, Y., Wu, S., Liu, R., 2022. Magnetically induced self-assembly DNAzyme electrochemical biosensor based on gold-modified α -Fe₂O₃/Fe₃O₄ heterogeneous nanoparticles for sensitive detection of Ni²⁺. *Nanotechnology* 33, 095601.
- Zhang, M., Cheng, S., Jin, Y., Zhao, Y., Wang, Y., 2021a. Roles of CA125 in diagnosis, prediction, and oncogenesis of ovarian cancer. *BBA-Rev. Cancer* 1875, 188503.
- Zhang, C., He, J., Zhang, Y., Chen, J., Zhao, Y., Niu, Y., Yu, C., 2018. Cerium dioxide-doped carboxyl fullerene as novel nanoprobe and catalyst in electrochemical biosensor for amperometric detection of the CYP2C19*2 allele in human serum. *Biosens. Bioelectron.* 102, 94–100.
- Zhang, Y.L., Ouyang, H.Z., Zhang, S.S., Ni, Y., Zhu, Z.Y., Ling, C., He, A.L., Liu, R.J., 2023. Label-free electrochemical bioplatfrom based on Au-modified magnetic Fe₃O₄/ α -Fe₂O₃ hetero-nanorods for sensitive quantification of ovarian cancer tumor marker. *Microchem. J.* 189, 108546.
- Zhang, R., Siu, M.K.Y., Ngan, H.Y.S., Chan, K.K.L., 2022a. Molecular biomarkers for the early detection of ovarian cancer. *Int. J. Mol. Sci.* 23, 12041.
- Zhang, X., Wang, Y., Deng, H., Xiong, X., Zhang, H., Liang, T., Li, C., 2021b. An aptamer biosensor for CA125 quantification in human serum based on up conversion luminescence resonance energy transfer. *Microchem. J.* 161, 105761.
- Zhang, S., Xu, S., Ni, Y., Zhu, Z., Ling, C., Liu, R., 2022b. Adsorption mechanism and electrochemical characteristic of methyl blue onto calcium ferrite nanosheets. *Adsorpt. Sci. Technol.* 2022, 6999213.
- Zhao, Y., Tao, Y., Huang, Q., Huang, J., Kuang, J., Gu, R., Zeng, P., Li, H., Liang, H., Liu, H., 2022. Electrochemical biosensor employing Bi₂S₃ nanocrystals-modified electrode for bladder cancer biomarker detection. *Chemosensors* 10, 48.